

CFD based simulations of flutter characteristics of ideal thin plates with and without central slot

Zhi-wen Zhu^{1,2}, Zheng-qing Chen¹ and Ming Gu^{2*}

¹Center of Wind Engineering, Hunan University, Changsha 410082, China

²State Key Laboratory for Disaster Reduction in Civil Engineering,
Tongji University, Shanghai 200092, China

(Received January 11, 2007, Accepted November 6, 2008)

Abstract. In this paper, the airflow around an ideal thin plate (hereafter referred to as ITP) with various ratios of central slot is simulated by using the finite-difference-method (FDM)-based Arbitrary-Lagrangian-Eulerian descriptions for the rigid oscillating body. The numerical procedure employs the second-order projection scheme to decouple the governing equations, and the multigrid algorithm with three levels to improve the computational efficiency in evaluating of the pressure equation. The present CFD method is validated through comparing the computed flutter derivatives of the ITP without slot to Theodorsen analytical solutions. Then, the unsteady aerodynamics of the ITP with and without central slot is investigated. It is found that even a smaller ratio of central slot of the ITP has notable effects on pressure distributions of the downstream section, and the pressure distributions on the downstream section will further be significantly affected by the slot ratio and the reduced wind speeds. Continuous increase of A_2^* with the increase of central slot may be the key feature of the slotted ITP. Finally, flutter analyses based on the flutter derivatives of the slotted ITP are performed, and moreover, flutter instabilities of a scaled sectional model of a twin-deck bridge with various ratios of deck slot are investigated. The results confirm that the central slot is effective to improve bridge flutter stabilities, and that the flutter critical wind speeds increase with the increase of slot ratio.

Keywords: ITP; central slot; CFD; projection-2 scheme; multigrid method; unsteady pressure; flutter.

1. Introduction

The concept of flutter derivatives was derived from aeronautical studies, which was first formulated in incompressible potential flow for a thin airfoil, with main contributions from Theodorsen (1935). This kind of thin airfoil with infinite aspect ratio and zero thickness is considered as an ITP in bridge aerodynamics. While in wind-resistant studies for bridges, flutter derivatives of the ITP can be used analogously in analyses of flutter instabilities of super-long span bridges with streamlined box girders. In addition, with respect to methodology study on identification of flutter derivatives based on sectional model tests, the flutter derivatives of the ITP are often employed as a benchmark to verify the effectiveness of presented method. However, the flutter derivatives of the ITP can't be perfectly obtained from wind tunnel tests, since it is idealized to be a

* Professor, Corresponding Author, E-mail: minggu@mail.tongji.edu.cn

rigid body with zero thickness. Common measures are realized along this way in wind tunnel tests: a thin plate sectional model with ratio of width to height of more than 20 as well as streamlined leading and trailing edges (Gu, *et al.* 2000). Flutter derivatives of this kind of sectional model obtained from wind tunnel tests will be treated as an approximation to those of the ITP. Obviously, agreement between the flutter derivatives of the thin plate model and those of the ITP will be highly dependent on the outline of the sectional model, test rigs, wind tunnel facilities and identification approach employed.

Suitable slotting on bridge girder is considered as an effective way to improve flutter stabilities of super-long span bridges. A typical example is the stiffening girder section of the Messina Strait Bridge which will connect the Sicilian Island to Italy mainland. Based on sectional model wind tunnel tests and analytical studies, Sato, *et al.* (1995, 2000) evaluated the effects of slot size and location on flutter instabilities of bridge decks, it was found that the central slot on the bridge girder was effective to improve the aerodynamic stabilities. However, the flutter critical wind speeds obtained from his analytical studies were slightly higher than those obtained from the wind tunnel tests, since the aerodynamic forces acting on both of the upstream and downstream sections were calculated from the Theodorsen's function, with neglected aerodynamic interference between them. Sato, *et al.* (2002) also validated the above conclusion through a full bridge aeroelastic model test. Matsumoto, *et al.* (1999) measured the unsteady wind pressures on two series of tandem rectangular cylinders with different spacing distances, and it was shown that even though the spacing distance was large, the unsteady pressure of the downstream cylinder was still significantly affected by the wake of the upstream cylinder, and the two series of tandem rectangular cylinders had rather stable characteristics against flutter instabilities. Based on vortex concept of the classical two-dimensional potential flow theory, Larsen, *et al.* (1998) presented a simple vortex model for determination of flutter critical wind speeds of twin-deck bridge sections, the effects of various ratios of central slot on the flutter wind speeds were also studied.

As a developing and promising approach to address problems in wind engineering, Computational Fluid Dynamics (CFD) methods have been widely used to deal with the bridge aerodynamics and aeroelasticity. Larsen and Walther (1997) as well as Walther and Larsen (1997) first developed a discrete vortex method, which is a grid-free algorithm and thus applicable to bluff body with relatively more complexity. The resultant program DVMFLOW was employed to study the effectiveness of various ratios of central slot on flutter stabilities for a twin-deck bridge, as well as the flutter prediction of multi-element bridge decks for Messina Strait Bridge (Larsen, *et al.* 1998). Shirai and Ueda (2003) predicted the flutter behaviors of bridge girder sections with a central slot by using the nonlinear $k - \varepsilon$ model, and the simulated flutter derivatives showed reasonable trend with those from wind tunnel tests. Based on ALE method, Frandsen (1999) employed FEM to solve fluid-structure coupled equations, with vortex-induced vibrations and flutter behaviors of practical bridge girders being studied. Jeong and Kwon (2003) also employed ALE-based FEM to solve flow field around a moving bridge section to obtain unsteady aerodynamic forces.

For the special physical model of the ITP, practical difficulties exist in wind tunnel tests to evaluate flutter derivatives of the ITP with various ratios of central slot, this paper thus adopts CFD procedures to deal with the problem. The present method consists of three steps. In the first step, the unsteady aerodynamics of the ITP without slot is simulated. In order to validate effectiveness of the numerical method, the identified flutter derivatives are compared with Theodorsen analytical solutions. In the second step, the flutter derivatives of the slotted ITP with slot ratios ranging from small value of 5% to large value of 90% are extracted, and some important features at different

reduced wind speeds are discussed. In the last step, based on the obtained flutter derivatives of the slotted ITP, flutter critical wind speeds of a scaled sectional model of a twin-deck bridge are investigated through two-degree-of-freedom flutter analyses, and are further compared with Larsen's results (1998). Compared with previous methods (Sato, *et al.* 1995, Larsen, *et al.* 1998), the present method simulates the viscous incompressible flow at a wide range of reduced wind speed, while the aerodynamic interference between the upstream and downstream sections can be fully considered. In addition, based on orthogonal structured grids and a multigrid algorithm, the present method can model the ITP with various ratios of central slot conveniently, leading to an effective prediction about the effects of different slot ratios on the flutter instabilities of the slotted ITP.

2. Theodorsen analytical solution

Flutter is one of self-excited oscillations powered by energy absorbed from airflow. The corresponding self-excited forces involved in the flutter are commonly expressed as linear functions of small amplitude sinusoidal displacements and their first derivatives weighed by flutter derivatives. Equations of aeroelastic lift and moment suggested by Scanlan and Tomko (1971) are employed for the ITP, with notations explained in Fig. 1.

$$L = \frac{1}{2}\rho U^2(2b) \left[kH_1^* \frac{\dot{h}}{U} + kH_2^* \frac{b\dot{\alpha}}{U} + k^2 H_3^* \alpha + k^2 H_4^* \frac{h}{b} \right] \quad (1)$$

$$M = \frac{1}{2}\rho U^2(2b^2) \left(kA_1^* \frac{\dot{h}}{U} + kA_2^* \frac{b\dot{\alpha}}{U} + k^2 A_3^* \alpha + k^2 A_4^* \frac{h}{b} \right) \quad (2)$$

where, L and M denote the self-excited lift and moment per unit length, respectively; ρ is the air density; b the half width of ITP; U the mean wind speed; h and α are the displacements of the ITP in heave and pitch, respectively. Eqs. (1) and (2) define the aeroelastic forces which depend on the displacements and velocities in terms of flutter derivatives H_i and A_i ($i=1,2,3,4$), which are functions of the reduced circular frequency $k = \omega b/U$.

The flutter derivatives of the ITP take the following forms (Theodorsen, 1935),

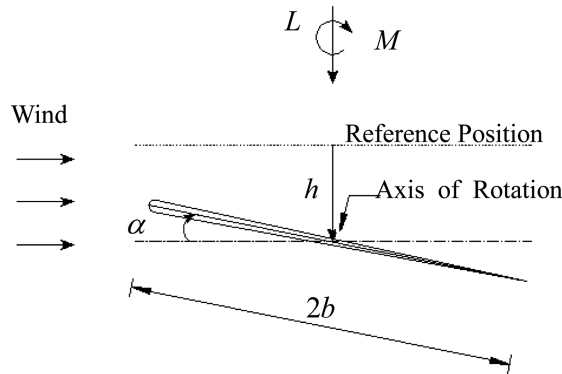


Fig. 1 Sketch of ITP in smooth flow with two degrees of freedom

$$\begin{aligned}
H_1^* &= -\frac{2\pi F(k)}{k}; & H_2^* &= -\frac{\pi}{k}\left(1 + F(k) + \frac{2G(k)}{k}\right); \\
H_3^* &= -\frac{2\pi}{k^2}\left(F(k) - \frac{kG(k)}{2}\right); & H_4^* &= \pi\left(1 + \frac{2G(k)}{k}\right); \\
A_1^* &= \frac{\pi F(k)}{k}; & A_2^* &= -\frac{\pi}{2k}\left(1 - F(k) - \frac{2G(k)}{k}\right); \\
A_3^* &= \frac{\pi}{k^2}\left(F(k) - \frac{kG(k)}{2}\right) + \frac{\pi}{8}; & A_4^* &= -\frac{\pi G(k)}{k}.
\end{aligned} \tag{3}$$

where $C(k) = F(k) + iG(k)$ is the Theodorson' s function.

3. Numerical method and implementation

3.1. The governing equations

Taking the advantage of both Lagrangian description and Eulerian description, the Arbitrary-Lagrangian-Eulerian description can deal with problems which can not be carried out either by Lagrangian description or Eulerian description, such as large amplitude boundary moving in computational domain. Noh (1964) first presented the ALE method based on a FDM scheme as to solve two dimensional fluid dynamical problems with moving boundaries. There are many reports followed using the ALE method to handle the fluid-structure interaction as well as nonlinear problems in solid mechanics where contact, impact and large deformation occur. If the ALE description applies to fluid-structure interaction with rigid boundaries, the governing equations can be largely simplified, as researches reported by Nomura (1992, 1994).

Based on the ALE description for a rigid oscillating body undergoing vertical heaving or torsional pitching motion, the laminar viscous incompressible flow around the ITP in a moving reference system is governed by the time-dependent Navier-Stokes Equations(NSEs) in computational domain as follows,

$$\frac{\partial u}{\partial t} + u_r \frac{\partial u}{\partial x} + v_r \frac{\partial u}{\partial y} + \frac{1}{\rho} \frac{\partial p}{\partial x} = \nu \left(\frac{\partial^2 u}{\partial x^2} + \frac{\partial^2 u}{\partial y^2} \right) - \omega v \tag{4a}$$

$$\frac{\partial v}{\partial t} + u_r \frac{\partial v}{\partial x} + v_r \frac{\partial v}{\partial y} + \frac{1}{\rho} \frac{\partial p}{\partial y} = \nu \left(\frac{\partial^2 v}{\partial x^2} + \frac{\partial^2 v}{\partial y^2} \right) + \omega u \tag{4b}$$

$$\frac{\partial u}{\partial x} + \frac{\partial v}{\partial y} = 0 \tag{4c}$$

where u and v denote the projection velocities of the airflow in horizontal and vertical axes, from the fixed reference system to the moving reference system, respectively; ω is the circular frequency about the central axis of rotation; p is the static pressure; ν is the kinematical viscosity; u_r , v_r are the

airflow velocities with reference to the moving coordinate system, and can be expressed as

$$u_r = u + V_0 \sin \psi - \omega y \quad (5a)$$

$$v_r = v - V_0 \cos \psi + \omega x \quad (5b)$$

It is evident that Eq.(4) is different from the classical NSEs, since the convective velocities in momentum equations are velocities with reference to the moving coordinate system, as described by Eq.(5). Moreover, a Coriolis force term is also added to right-hand side of each momentum equation, which accounts for an inertial force induced by the body's pitching motion.

3.2. Temporal discretization

A significant difficulty for solving the above unsteady NSEs occurs since the continuity equation is given not in a time evolution form, but in a form of a divergence-free constraint. This is one of the major differences from compressible flow calculations. The pressure, which has no time terms, is coupled implicitly with the divergence-free constraint on the velocity. This constraint, which is the continuity equation, prohibits time integration of the incompressible flow equations in a straightforward manner. A method, which is known as the projection method, has been developed by Chorin (1968) and is now widely used to calculate the incompressible flow. Roughly speaking, the projection method is based on the following philosophy: in incompressible flow, the pressure does not carry any thermodynamic meaning and is presented only as a Lagrange multiplier for the incompressibility constraint. This observation motivates a time-splitting scheme of discretization which decouples the computation of velocity and pressure. This is the key feature of the projection method. In the first step, an intermediate velocity field is computed by using the momentum equations and ignoring the incompressibility constraint; and in the second step, the intermediate velocities are projected to the space of divergence-free vector fields to get the next update of velocities and pressure. This procedure is much more efficient than solving a coupled system of Stokes equations for velocities and pressure which would arise from a straightforward temporal discretization of the NSEs.

The projection method is comprised of two schemes, namely the first-order Projection-1 scheme and the second-order Projection-2 scheme (Bell, *et al.* 1989). If Eq.(4) is decoupled by using the Projection-2 scheme, a second-order semi-implicit discretization can be written as follows,

1) The momentum equations for the intermediate velocities,

$$\frac{3\tilde{u}^{k+1} - 4u^k + u^{k-1}}{2\Delta t} + \tilde{u}_r^{k+1} \frac{\partial \tilde{u}^{k+1}}{\partial x} + \tilde{v}_r^{k+1} \frac{\partial \tilde{u}^{k+1}}{\partial y} + \frac{1}{\rho} \frac{\partial p^k}{\partial x} = \nu \left(\frac{\partial^2 \tilde{u}^{k+1}}{\partial x^2} + \frac{\partial^2 \tilde{u}^{k+1}}{\partial y^2} \right) - \omega \tilde{v}^{k+1} \quad (6a)$$

$$\frac{3\tilde{v}^{k+1} - 4v^k + v^{k-1}}{2\Delta t} + \tilde{u}_r^{k+1} \frac{\partial \tilde{v}^{k+1}}{\partial x} + \tilde{v}_r^{k+1} \frac{\partial \tilde{v}^{k+1}}{\partial y} + \frac{1}{\rho} \frac{\partial p^k}{\partial y} = \nu \left(\frac{\partial^2 \tilde{v}^{k+1}}{\partial x^2} + \frac{\partial^2 \tilde{v}^{k+1}}{\partial y^2} \right) + \omega \tilde{u}^{k+1} \quad (6b)$$

2) The Poisson equation governing the pressure field,

$$\left(\frac{\partial^2 p^{k+1}}{\partial x^2} + \frac{\partial^2 p^{k+1}}{\partial y^2} \right) - \left(\frac{\partial^2 p^k}{\partial x^2} + \frac{\partial^2 p^k}{\partial y^2} \right) = \frac{3\rho}{2\Delta t} \left(\frac{\partial \tilde{u}^{k+1}}{\partial x} + \frac{\partial \tilde{v}^{k+1}}{\partial y} \right) \quad (7)$$

3) And the equations for corrected velocities,

$$u^{k+1} = \tilde{u}^{k+1} - \frac{2\Delta t}{3\rho} \left(\frac{\partial p^{k+1}}{\partial x} - \frac{\partial p^k}{\partial x} \right) \quad (8a)$$

$$v^{k+1} = \tilde{v}^{k+1} - \frac{2\Delta t}{3\rho} \left(\frac{\partial p^{k+1}}{\partial y} - \frac{\partial p^k}{\partial y} \right) \quad (8b)$$

where \tilde{u} and \tilde{v} are the intermediate velocities, corresponding to u and v , respectively; $k+1$ the current time step. For temporal discretization at the first time step, an Euler back-difference representation is employed to avoid initial conditions at $k-1$ time step.

3.3. Spatial discretization

In the present paper, staggered structured grids are used to discretize the governing equations spatially, in which the velocities are defined on cell boundary centers while the pressure defined at the cell center. Such a configuration ensures that the difference representation for the divergence is of conservative property. At the same time, the pressure difference between the adjacent grid points becomes a natural driving force for velocity components located midway between the grid points. Moreover, solid boundary conditions for pressure are not needed, which is more important for the Projection-2 scheme. The outer boundaries of computational domain are located away from the ITP with enough distances, while the number of grids in each direction should be prescribed so that a multigrid algorithm can be implemented conveniently.

Compared with the velocity of incoming flow in the CFD simulations, moving velocity of the ITP will be very low. Hence the relative angle of attack between the ITP and incoming flow will be very small. Consequently, violent separation may not occur in the flow field around the ITP for the simulations which are performed under low Reynolds number. Accordingly, the parabolic operator in Eq.(6) is approximated by a second-order central difference scheme, while the convective terms are approximated by a second-order Adams-Bashforth scheme to avoid solving a nonlinear system at each time step. For example, the convective terms in Eq.(6a) can be represented as,

$$\frac{\partial \tilde{u}^{k+1}}{\partial x} = \frac{1}{2} \left(3 \frac{\partial \tilde{u}^k}{\partial x} - \frac{\partial \tilde{u}^{k-1}}{\partial x} \right) \quad (9a)$$

$$\frac{\partial \tilde{u}^{k+1}}{\partial y} = \frac{1}{2} \left(3 \frac{\partial \tilde{u}^k}{\partial y} - \frac{\partial \tilde{u}^{k-1}}{\partial y} \right) \quad (9b)$$

in which the spatial derivatives at time step k and $k-1$ are approximated by a second-order central difference scheme.

This three-level time scheme of the convective terms is compatible with the time scheme of Projection-2 employed in Eq.(6). The second-order partial derivatives for pressure are also discretized by a central difference scheme. For incompressible NSEs, numerous numerical experiments and theoretical justification indicate that such treatments for the spatial discretization of the variables do not affect the second-order time accuracy for the velocities (Lopez and Shen, 1998).

3.4. Multigrid method

After temporal and spatial discretization of Eq.(4), the obtained difference equations can be solved

by using an iterative method, such as the Line Gauss-Seidal iterative method. However, it is time-consuming to solve these equations by an iterative method, especially to solve Eq. (7). This Poisson-type pressure equation converges painfully slowly when the Gauss-Seidal iteration is employed, because the Gauss-Seidal iteration can only provide excellent smoothing of the local error, and a very large number of iterations are often required for the influence of boundary conditions to propagate throughout the computational domain.

Nowadays, the multigrid method (Brandt, 1977) is widely adopted for solution of algebraic systems resulting from discretization of system of partial differential equations. The ideal of the multigrid is the use of successively coarser grids to compute correction to a fine grid solution. It is commonly observed that the iterative error consists of components with various frequencies. It is the removal of the low-frequency components of the error that usually slows convergence of the iterative scheme on a fixed grid. However, a low-frequency component on a fine grid becomes a high-frequency component on a coarse grid. Therefore, it makes good sense to use coarse grids to remove the low-frequency errors and propagate boundary conditions throughout the domain in combination with fine grids to improve the accuracy.

In the present paper, a “V” cycle iteration of the multigrid algorithm with three kinds of grid levels, i.e., the finest grid level 1 with grids of 106×82 , the coarser grid level 2 with grids of 54×42 and the coarsest grid level 3 with grids of 28×21 , is employed to improve the iterative convergence rate of the pressure equation. For this grid arrangement, every second fine grid will be a coarse grid.

The difference equation obtained from the discretization of Eq. (7) can be written in the following form,

$$Lp_{i,j} = S_{i,j} \quad (10)$$

where p denotes the pressure; L is the difference operator; $S_{i,j}$ is the source term consisting of all the known terms moved to the right-hand side of equation. Eq.(10) represents the pressure relationship between the point (i,j) and its neighboring points.

The final iterative solution, $p_{i,j}$ in Eq. (10), can be written as the sum of an intermediate solution, $p_{i,j}^k$, and a correction, $\Delta p_{i,j}$, i.e.,

$$p_{i,j} = \Delta p_{i,j} + p_{i,j}^k \quad (11)$$

where k denotes the iterative level. Substituting Eq.(11) into Eq.(10), one obtains,

$$L\Delta p_{i,j} + Lp_{i,j}^k = S_{i,j} \quad (12)$$

The intermediate solution may not satisfy Eq.(10), therefore, a residual may appear, and can be expressed as,

$$Lp_{i,j}^k - S_{i,j} = R_{i,j} \quad (13)$$

where $R_{i,j}$ is the residual. Substituting Eq.(13) into Eq.(12), one obtains,

$$L\Delta p_{i,j} = -R_{i,j} \quad (14)$$

Eq.(14) is known as the residual form of Eq.(10), and can be solved iteratively for $\Delta p_{i,j}$ until convergence. If $p_{i,j}$ and $R_{i,j}$ are updated after each iteration, the correction will gradually become small and finally vanish upon convergence.

The multigrid algorithm implemented in the present paper can be outlined as the following steps (Tannehill, *et al.* 1997):

- 1) Eq.(10) is iterated 3 times on the grid level 1 with the Line Gauss-Seidal scheme as a “smoother”, no overrelaxation is used. The residual is computed and stored at each point on the grid level 1.
 - 2) The residual is then restricted directly to the grid level 2 by “injection”, and Eq.(14) is iterated 3 times on the grid level 2 by using zero as the initial guess while keeping the residual fixed at each grid point. Δp_{ij} obtained from iterations on the grid level 2 represents a correction to p_{ij} on the grid level 1. In order to transfer the problem to the grid level 3, an updated residual is computed on the grid level 2, and is directly restricted to the grid level 3.
 - 3) Eq.(14) is iterated 3 times on the grid level 3, and the iterative solution can be thought as a correction to the correction obtained on the grid level 2, which represents a further correction to the finest-grid solution on the grid level 1.
 - 4) The corrections obtained on the grid level 3 are interpolated to the grid level 2, and then added to the corrections obtained earlier on the grid level 2 in the restriction phase. The sum of the two corrections is used as the initial guess at each point to solve Eq.(14) on the grid level 2, and the solution after 3 iterations represents the improved correction.
 - 5) The corrections from the grid level 2 are interpolated to the grid level 1, and added to the last solution, p_{ij} , obtained on the grid level 1. The corrected solution is then iterated 3 times unless convergence is detected before the iterations are completed.
 - 6) If the convergence does not occur on the grid level 1, the above steps will be repeated.
- The use of multigrid technique in this paper is capable of substantially improving the convergence rate in solving the pressure equation, leading to a significant reduction in computing time.

3.5. Solution conditions and numerical implementation

To obtain the unsteady aerodynamic forces acting on the oscillating ITP, two series of simulations are performed separately when the ITP is forced to oscillate sinusoidally with only 1DOF, i.e., pure heave or pure pitch. Accordingly, the ITP should be forced to pitch in a prescribed harmonic mode about its axis of rotation, namely,

$$\alpha(t) = \alpha_0 \sin(\omega_\alpha t) \quad (15a)$$

or heave vertically as,

$$h(t) = h_0 \sin \omega_h t \quad (15b)$$

where ω_α and ω_h denote the corresponding circular frequencies, respectively; α_0 a small constant amplitude of the torsional DOF; h_0 a small constant amplitude of the vertical DOF. In the present

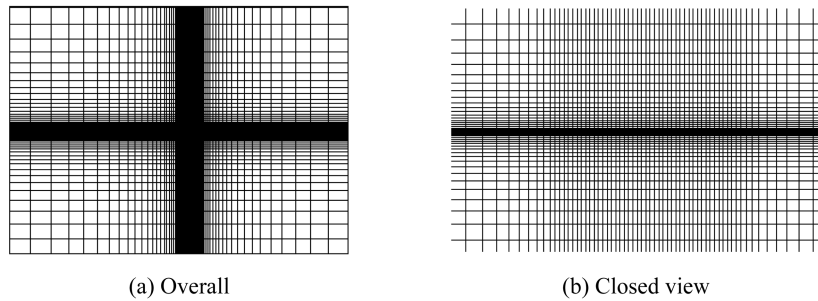


Fig. 2 Grids system around ITP

simulations, vertical and torsional amplitudes are set to $0.05b$ and 3° , respectively.

In application of CFD method to a practical simulation, the physical domain must be first covered with a suitable mesh. Here, the orthogonal structured mesh is employed. The computational domain is a rectangle, with the distances from its outer boundaries to the center of the ITP more than 20 times the width of the ITP, as indicated in Fig. 2. There are 106 grids distributed on the grid lines which are parallel to the ITP, while 82 grids on the grid lines normal to the ITP. 40 grids with a uniform space of $0.05b$ are arranged on each surface of the ITP. The minimum grid space is about $0.01b$ in the normal direction near the wall. Since CFD studies (Frandsen, 1999, zhu, *et al.* 2007) show that flutter derivatives of bridge decks are not sensitive to Reynolds number, based on the characteristic length of $2b$ and the incoming flow velocity, the airflow around the ITP will be simulated at a Reynolds number of about 600, and the corresponding time step is set to $0.01b/U$.

Since the mesh moves with the ITP synchronously at each time step, the grids' velocities are prescribed. The no-slip and no-penetration conditions can be applied to the surface of the ITP, and the incoming wind speed is projected on the inlet boundary. For the Projection-2 scheme, it is found that the boundary layer structures are strongly influenced by the numerical boundary conditions for the pressure at the projection step. For example, Dirichlet boundary conditions for the pressure lead to lower order of numerical boundary layers for the pressure, and deteriorate accuracy in interior of the computational domain, while analysis favors strongly the choice of Neumann boundary conditions (Bell, *et al.* 1989). With the use of staggered grids, it is easy to apply Neumann boundary conditions.

At certain time step, Eqs.(6) ~ (8) can be solved by following the flowchart shown in Fig. 3. The intermediate velocities are calculated from the momentum (Eq.(6)), with the pressure field obtained at the last time step. Then the Poisson-type equation is solved to obtain the pressure field at current time step, by virtue of the known intermediate velocities. Then, the intermediate velocities are corrected to obtain corrected velocities. Above operations will be repeated until the divergence of

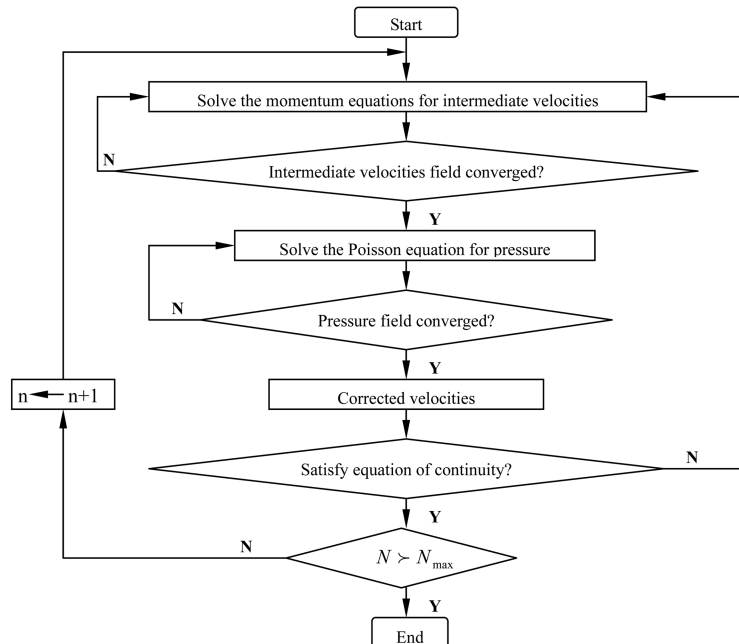


Fig. 3 Flowchart of Projection-2 scheme

velocity is small enough at this time step.

3.6. Unsteady aerodynamic forces and flutter derivatives

Define the downward direction of lift and the nose-up direction of moment to be positive, the lift and moment coefficients take the common forms as follows,

$$C_L = 2L/(\rho U^2 \cdot 2b) \quad (16a)$$

$$C_M = 2M/(\rho U^2 \cdot 4b^2) \quad (16b)$$

Figs. 4 and 5 are time histories of the lift and moment coefficients of the ITP oscillating in heave or pitch in wind at reduced wind speed $V_r = U/(fb) = 4$. All of these data are collected after 1.25 cycles of simulations. These time histories show sinusoidal manner vs. non-dimensional time

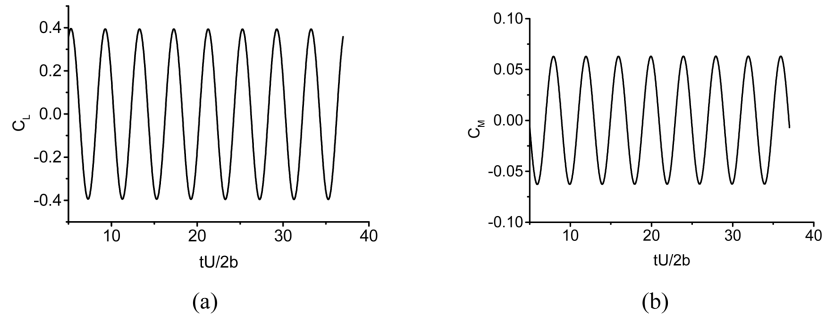


Fig. 4 Time histories of aerodynamic coefficients of ITP oscillating in heave at $V_r = 4$

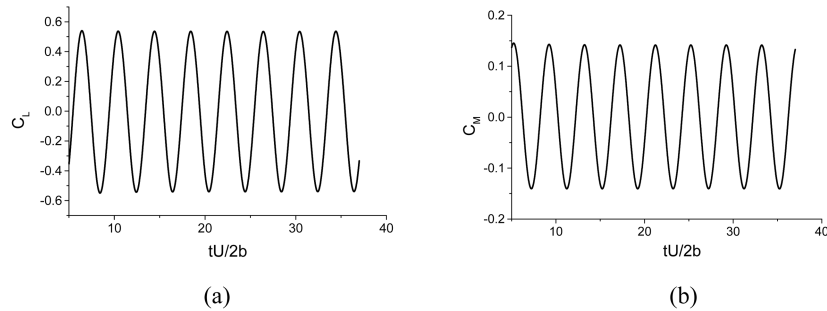


Fig. 5 Time histories of aerodynamic coefficient of ITP oscillating in pitch at $V_r = 4$

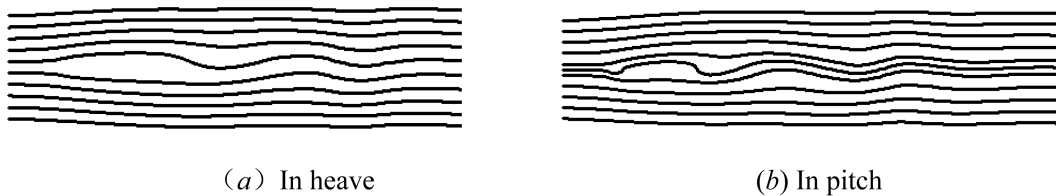


Fig. 6 Instantaneous streamline plots around ITP

$t^* = tU/(2b)$, and no recognizable fluctuation appears, indicating linear relationships between the aerodynamic forces and the displacement of the ITP.

Fig. 6 is the instantaneous streamline plots around the ITP at $T/4$ (T is the oscillating period) when it is oscillating in heave or pitch at $V_r = 4$. One can see that no pronounced separation occurs in flow fields. The streamlines in the wake clearly show the unsteady feature of airflow caused by the oscillating ITP.

Figs. 7 and 8 are the pressure contour plots around the ITP at four key states, where (a), (b) and (c) correspond to the elapsing time at $T/4$, $T/2$ and $3T/4$, respectively, while (d) corresponds to the elapsing time when the ITP moves back to reference positions. The figures clearly show that

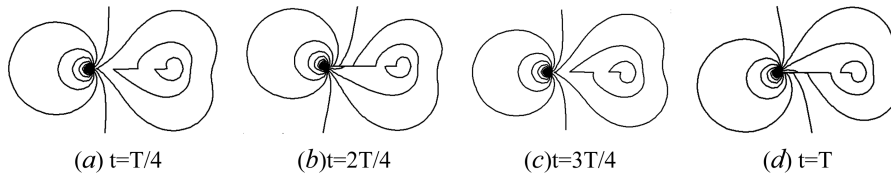


Fig. 7 Pressure contour plots around ITP oscillating in heave at $V_r = 4$

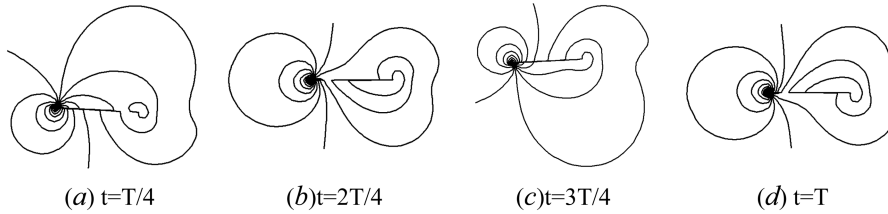


Fig. 8 Pressure contour plots around ITP oscillating in pitch at $V_r = 4$

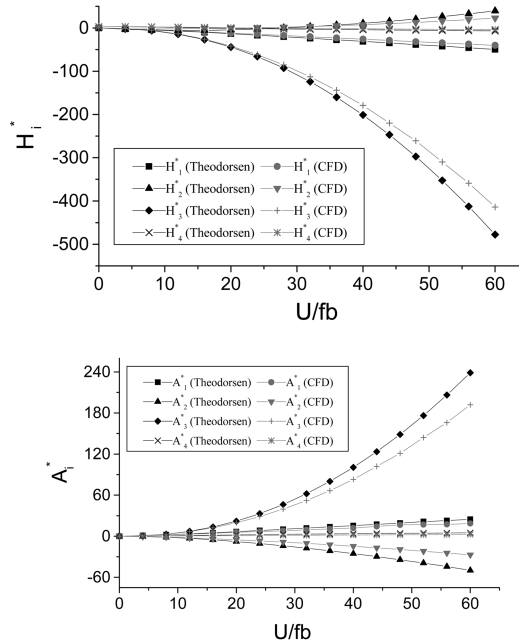


Fig. 9 Simulated flutter derivatives of ITP in comparison with Theodorsen analytical solutions

pressure peaks appear near leading edges of the ITP, where stagnation points of pressure are included, and the pressure contours change regularly during an oscillating cycle.

After aerodynamic forces acting on the ITP at each time step are collected, the flutter derivatives can be extracted by using least square algorithm. The flutter derivatives of the ITP without slot at different reduced wind speeds are evaluated and shown in Fig. 9, together with Theodorsen analytical solutions. The simulated values seem to be in reasonable agreement with Theodorsen analytical solutions. The results indicate that the present method is capable of modeling the flow field around the ITP if the ITP oscillates with small amplitude. In the next section, the present method will be used to simulate the flow field around the ITP with various ratios of central slot.

4. Flutter derivatives of ITP with various central slot ratios

When the ITP immerses in incoming airflow, the airflow can be divided into two parts after the leading edge. Different flow patterns between the upper and lower regions would produce pressure differences around the ITP. As a result, aerodynamic lift and moment are induced. Naturally, the larger the pressure difference appears, the larger the lift and moment forces will be. From the following simulations, it can be seen that a central slot on the ITP can effectively reduce pressure differences between the upper and lower surfaces of the ITP, resulting in direct decrease in lift and moment forces.

Define the slot ratio r as

$$r = \frac{s}{2b} \times 100\% \quad (17)$$

where b is the solid width of upstream or downstream sections, and s is the net distance between them, as shown in Fig. 10. This definition of slot ratio is different from that in (Sato, *et al.* 2006). Based on the present definition, different slot ratios can be obtained through changing the net distance, which is convenient to model the ITP with various ratios of central slot. Nine cases, as

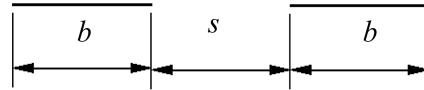


Fig. 10 CFD model of ITP with central slot

Table 1 Simulation cases of ITP with various ratios of central slot

Simulation case	(a)	(b)	(c)	(d)	(e)	(f)	(g)	(h)	(i)
Slot ratio (%)	0	5	10	20	30	40	50	60	90

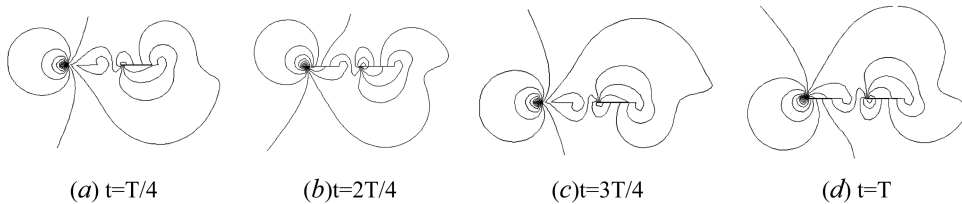


Fig. 11 Pressure contour plots around heaving ITP with slot ratio of 25% at $V_r = 4$

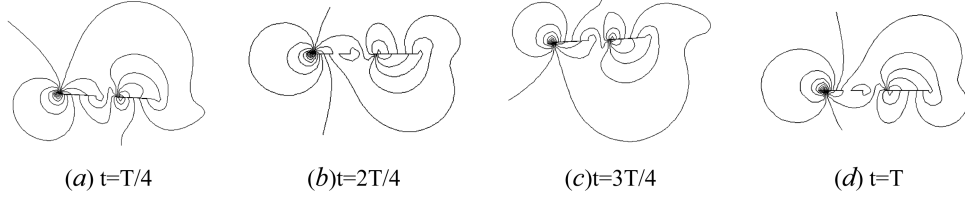


Fig. 12 Pressure contour plots around pitching ITP with slot ratio of 25% at $V_r = 4$

listed in Table 1, will be employed to investigate the effects of slot ratio on flutter derivatives and flutter characteristics of the slotted ITP.

Numerical simulations for the flow field around the ITP with central slot can be dealt with straightforward using the CFD method mentioned above. Then the aerodynamic behaviors can be investigated by examining the instantaneous pressure contours. Plotted in Figs. 11 and 12 are the pressure contours around the ITP with slot ratio of 25%, which is oscillating sinusoidally in heave or pitch respectively at the same moments as those in Figs. 7 and 8. One can see that some of the pressure contours run through the central slot, indicating small pressure differences or even identical pressures around the slot.

The unsteady pressure characteristics, or the amplitudes of pressure coefficients, $\overline{C_p}$, during a full cycle of torsional oscillation, are shown in Fig. 13. For all cases of the ITP with central slot, the amplitudes of pressure coefficients of the upstream section are almost identical to those of the ITP without slot. However, the amplitudes of pressure coefficients on the downstream section vary with slot ratio. Compared with the case of the ITP without slot, a smaller ratio of central slot, such as 5%, has notable effects on the pressure field, leading to the increase of pressure amplitudes on the downstream section. Meanwhile, one can see that at a given reduced wind speed, the pressure amplitudes on the downstream section will gradually increase with the increase of central slot. When the ITP with large central slot ratio, such as larger than 40%, oscillates at lower reduced wind speeds, such as 10, the distributions of pressure amplitudes on the downstream section are almost identical to those on the upstream section. One the other hand, for larger slot ratios, the unsteady pressure amplitudes on the downstream section will be gradually reduced with the increase of the reduced wind speed.

The flutter derivatives of the ITP with various slot ratios are obtained using the present method and are shown in Fig. 14. From the figure it can be seen that with the increase of the reduced wind speed, almost all the flutter derivatives of the ITP share the same variation trend with the reduced wind velocity. If further insights are given into Fig. 14, the variation of all flutter derivatives could be classified into two categories. The first category includes H_1^* , H_2^* , H_3^* , H_4^* , A_1^* and A_3^* ; and the second category includes A_2^* and A_4^* . For the first category, there are clear differences between the flutter derivatives of the ITP with and without central slot, even in the case of a small slot ratio of 5%, and furthermore, these differences do not vary significantly with the increase of central slot ratio. For the second category, no obvious differences can be found between flutter derivatives of the ITP without slot and those of the ITP with small slot ratios; however, with the increase of central slot ratio, the absolute values of the flutter derivatives show continuous increase, especially for A_2^* , which might be the key feature of the slotted ITP.

5. Flutter instability of ITP with central slot ratios

In order to evaluate the effects of slot ratio on flutter instabilities of the ITP, the flutter critical

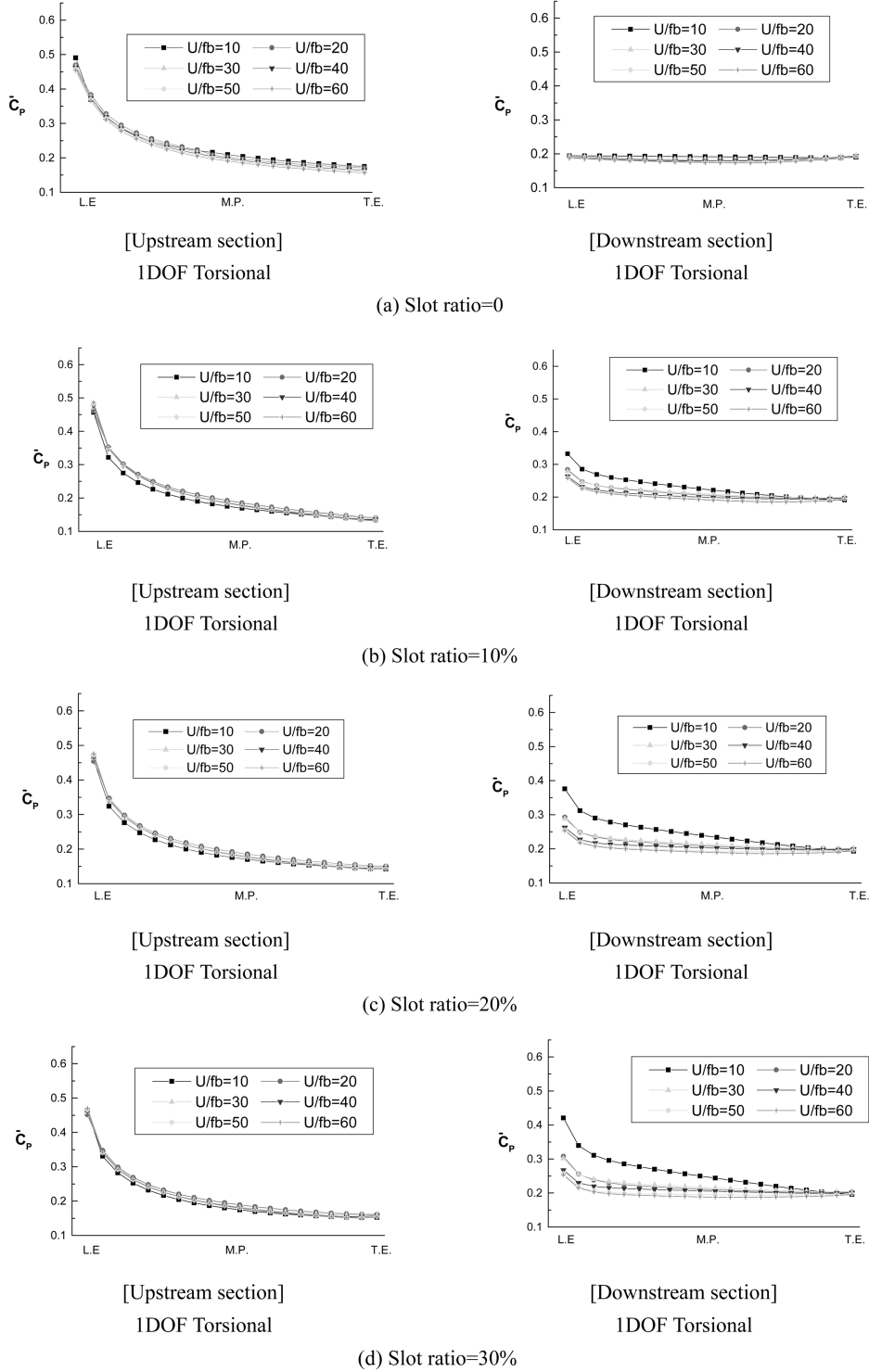


Fig. 13 Unsteady pressure distributions on ITP with various ratios of central slot

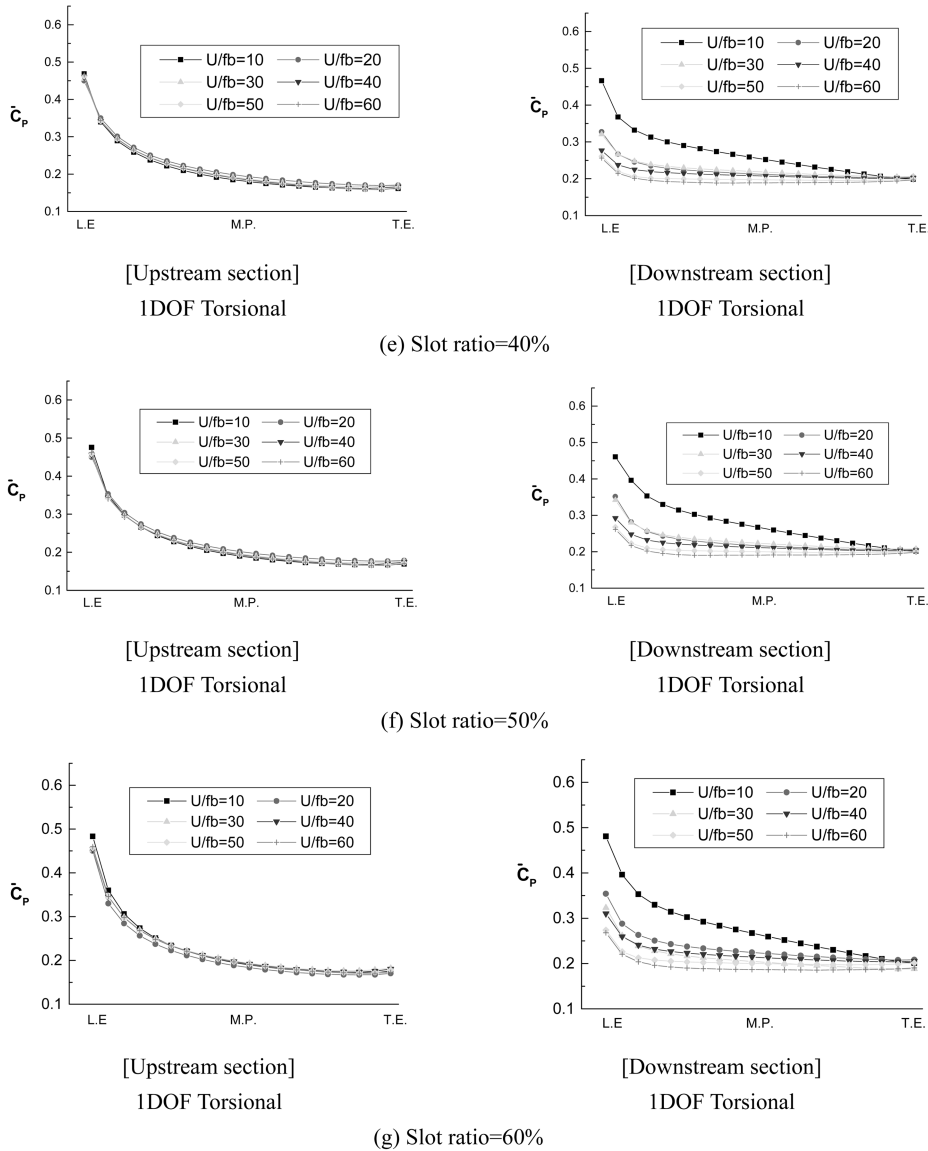


Fig. 13 Continued

wind speeds of a bridge deck which is similar to the ITP with central slot are computed. A 1:80 scaled sectional model of the Gibraltar Strait Crossing (Larsen, *et al.* 1998), a twin-deck stiffening girder with a wide central slot, is used, as shown in Fig. 15. The model has a ratio of width to thickness of 27. Streamlined fairings attached to both its leading and trailing edges make it a more streamlined slotted box girder. The structural parameters of the model are: deck solid width, $2b = 0.42$ meters; mass per unit length, $m = 6.17$ kg; mass moment of inertia per unit length, $I_0 = 0.56$ kgm^2 ; the first bending and torsional frequencies, f_h and f_{ω} are 1.08Hz and 1.58Hz, respectively; both the vertical and torsional damping ratios are assumed to be 0.005. As for the effects of variation of the slot ratio on the structural parameters, it is assumed that the vertical and

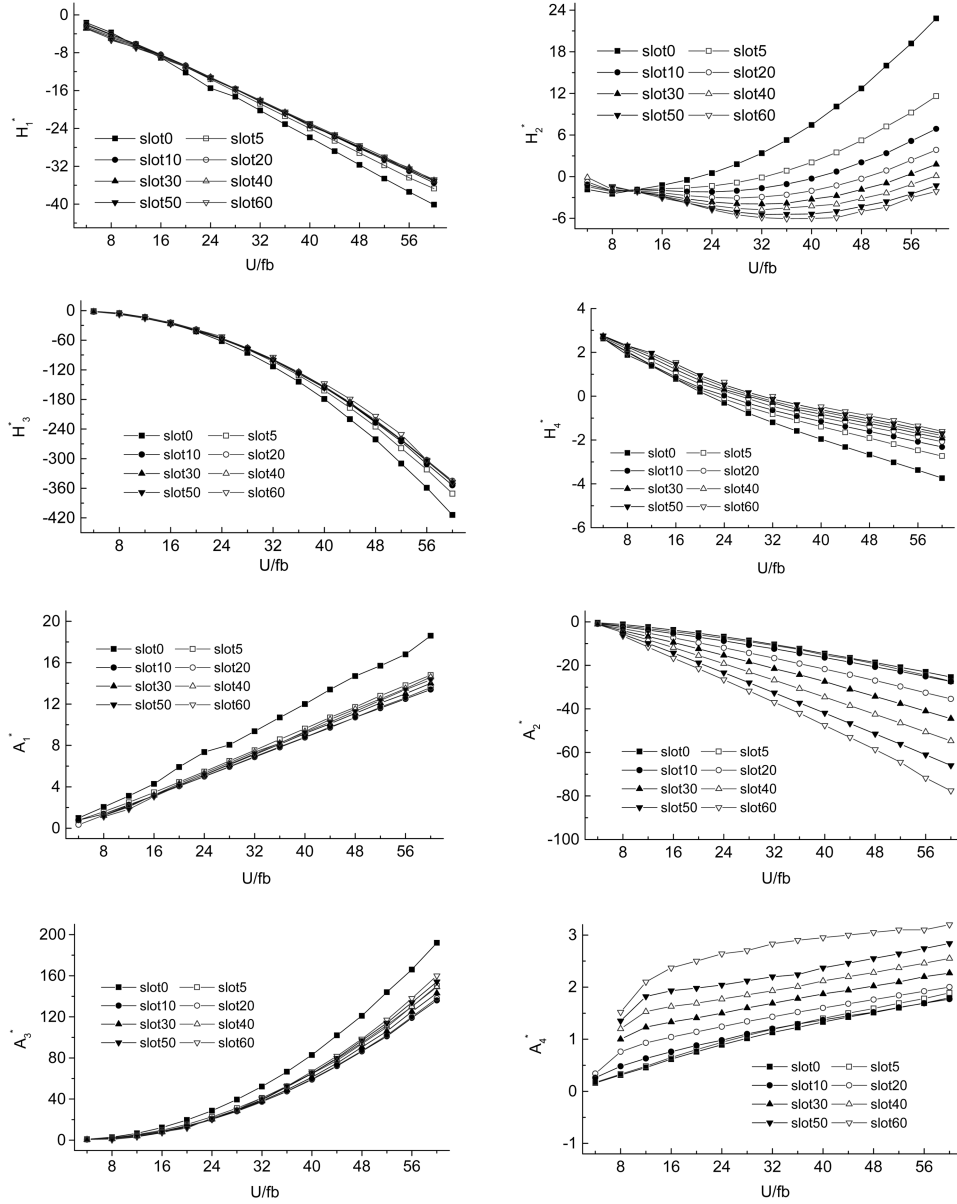


Fig. 14 Simulated flutter derivatives of ITP with various ratios of central slot

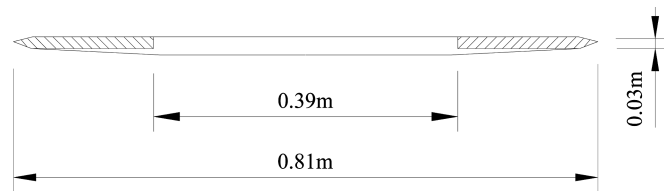
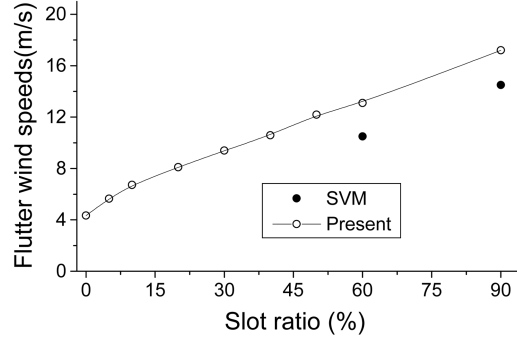


Fig. 15 Sketch of a scaled twin-deck sectional model (Larsen, *et al.* 1998)

Table 2 Bridge flutter critical wind speeds U_{cr} at different ratio of central slot (m/s)

Slot ratio(%)	0	5	10	20	30	40	50	60	90	Theodorsen
X	1.25	1.225	1.222	1.215	1.213	1.212	1.21	1.209	1.208	1.22
U/fb	15.3	20.3	24.2	29.4	34.1	38.5	44.4	47.8	63	16.4
U_{cr}	4.34	5.65	6.72	8.1	9.39	10.59	12.19	13.1	17.2	4.54


 Fig. 16 Flutter wind speeds of twin-deck section model in comparison with analytical results (Larsen, *et al.* 1998) for various ratios of central slot

torsional frequencies as well as mass per unit length are invariable, while the mass moment of inertia varies linearly with the width of central slot, s , in the following way:

$$I = m \cdot \left(\sqrt{\frac{I_0}{m}} - \frac{s_0}{2} + \frac{s}{2} \right)^2 \quad (18)$$

where $s_0 = 0.39$ (Larsen, *et al.* 1998)

Define the non-dimensional frequency X as

$$X = f/f_h \quad (19)$$

where f is the frequency to be determined in flutter analysis.

The Theodorsen's method (Theodorsen, 1935) for solving the flutter instability equations based on trial-and-error is employed to determine flutter conditions, including reduced wind speed U/fb and non-dimensional flutter frequency. The flutter conditions and critical wind speeds of the model with various ratios of central slot are given in Table 2. The results in Table 2 indicate that the flutter critical wind speed of the ITP without slot is in reasonable agreement with that obtained from Theodorsen analytical solutions, and the flutter critical wind speeds increase almost linearly with the increase of slot ratio, which can also be seen from Fig. 16.

In Fig. 16, Larsen's analytical results of the twin-deck bridge model with two kinds of central ratios of 60% and 90% (Larsen, *et al.* 1998) are also presented. The corresponding critical wind speeds are 10.5 m/s and 14.5 m/s, respectively, obviously lower than the present results. The difference between the present result and Larsen's result might be attributed to the different analytical models employed.

6. Concluding remarks

A CFD approach, based on the Arbitrary-Lagrangian-Eulerian descriptions for rigid oscillating

body and the finite difference discretization in combination with multigrid algorithm, is employed to investigate the flow field around an ITP with and without central slot at low Reynolds number of 600. The present method is verified through comparison of the simulated flutter derivatives of the ITP without slot with those of Theodorsen analytical solutions. The effects of slot ratio on the unsteady aerodynamics and the flutter instabilities are then investigated through applying the present CFD method to the ITP with various ratios of central slot. The main conclusion obtained in this study is summarized as follows:

(1) Central slot on the ITP has great effects on the unsteady pressure distributions of the downstream section of the ITP at all the reduced wind speeds; even through the ratio of central slot is very small.

(2) At certain reduced wind speed, the pressure amplitudes on the downstream section gradually increase with the increase of central slot. For larger slot ratios, the unsteady pressure amplitudes on the downstream section will gradually decrease with the increase of the reduced wind speeds.

(3) There are clear differences in some identified flutter derivatives H_1^* , H_2^* , H_3^* , H_4^* , A_1^* and A_3^* between the ITP with and without central slot, while the differences don't vary significantly with the increase of central slot ratio. On the other hand, the absolute values of A_2^* show continuous increase with the increase of central slot ratio, which may be a key feature of the slotted ITP.

(4) According to the flutter analyses based on the obtained flutter derivatives of the slotted ITP, it is confirmed that the central slot is effective to improve bridge flutter stabilities, and the flutter critical wind speeds increase with the increase of slot ratio.

Acknowledgements

Financial support for this study is provided by China National Science Foundation (50678067, 50478051, 50621062, 50308022), to which the writers gratefully appreciate.

References

- Bell, J., Colella, P. and Glaz, H. (1989), "A second-order projection method for incompressible Navier-Stokes equation", *J. Comput. Phys.*, **85**, 257-283.
- Brandt, A. (1977), "Multilevel adaptive solutions to boundary value problems", *Math. Comput.*, **31**, 333-390.
- Chorin, A.J. (1968), "Numerical solution of the Navier-Stokes equations", *Math. Comput.*, **22**, 745-762.
- Frandsen, J.B. (1999), "Computational fluid-structure interaction applied to long-span bridge design", PhD thesis, University of Cambridge, Cambridge.
- Gu, M., Zhang, R. X. and Xiang, H. F. (2000), "Identification of flutter derivatives of bridge decks", *J. Wind Eng. Ind. Aerod.*, **84**, 151-162.
- Jeong, U.Y. and Kwon, S.D. (2003), "Sequential numerical procedures for predicting flutter velocity of bridge sections", *J. Wind Eng. Ind. Aerod.*, **91**, 291-305.
- Larsen, A. and Walther, J.H. (1997), "Aeroelastic analysis of bridge girder sections based on discrete vortex simulations", *J. Wind Eng. Ind. Aerod.*, **67&68**, 253-265.
- Larsen, A., Vejrum, T. and Esdahl, S. (1998), "Vortex models for aeroelastic assessment of multi element bridge decks, Bridge aerodynamics", Larsen & Esdahl(eds), Balkema, Rotterdam.
- Lopez, J.M. and Shen, J. (1998), "Numerical simulation of incompressible flow in cylindrical geometries using a spectral projection method", *Int. J. Appl. Sci. & Comput.*, **5**, 25-40.
- Matsumoto, M., Yoshizumi, F. and Yabutani, T., *et al.* (1999), "Flutter stabilization and heaving-branch flutter", *J. Wind Eng. Ind. Aerod.*, **83**, 289-299.
- Noh, W.F. (1964), "A time dependent two space dimensional coupled Eulerian-Lagrangian code", *Methods in Comput. Phys., Fundamental Methods in Hydrodynamics*, B.Alder, S.Fernbach, M.Rotenberg, eds., Academic

- Press, New York, NY, **3**, 117-179.
- Nomura, T. and Hughes, T.J.R. (1992), "An arbitrary Lagrangian-Eulerian finite element method for interaction of fluid and a rigid body", *Comput. Methods Appl. M.*, **95**, 115-138.
- Nomura, T. (1994), "ALE finite element computations of fluid-structure interaction problems", *Comput. Methods Appl. M.*, **112**, 291-308.
- Sato, H., Hirahara, N. and Fumoto, K., *et al.* (2002), "Full aeroelastic model test of a super long-span bridge with slotted box girder", *J. Wind Eng. Ind. Aerod.*, **90**, 2023-2032
- Sato, H., Kusuhara, S. and Ogi, K., *et al.* (2000), "Aerodynamic characteristics of super long-span bridges with slotted box girder", *J. Wind Eng. Ind. Aerod.*, **88**, 297-306.
- Sato, H., Toriumi, R. and Kusakabe, T. (1995), "Aerodynamic characteristics of slotted box girders", *Proc. of Bridge into the 21st Century*, Hong Kong, 721-728.
- Scanlan, R.H. and Tomko, J.J. (1971), "Airfoil and bridge deck flutter derivatives", *J. Eng. Mech.*, ASCE, **97**, 1171-1173.
- Shirai, S. and Ueda, T. (2003), "Aerodynamic simulation by CFD on flat box girder of super-long-span suspension bridge", *J. Wind Eng. Ind. Aerod.*, **91**, 279-290.
- Tannehill, J.C., Anderson, D.A. and Pletcher, R.H. (1997), "Computational fluid mechanics and heat transfer (second edition)", Taylor & Francis, Washington, D.C., 165-176.
- Theodorsen, T. (1935), "General theory of aerodynamic instability and the mechanism of flutter", *NACA Report*, U.S. Nat. Advisory Committee for Aeronautics, Langley, Va, **496**.
- Walther, J.H. and Larsen, A. (1997), "2D Discrete vortex method for application to bluff body aerodynamics", *J. Wind Eng. Ind. Aerod.*, **67&68**, 183-193.
- Zhu, Z.W., Gu, M. and Chen, Z.Q. (2007), "Wind tunnel and CFD study on identification of flutter derivatives of a long-span self-anchored suspension bridge", *Comput.-Aided Civ. Inf.*, **22**, 541-554.